Proof-of-Concept Experiment of Microfluidic Flow Sensor Based on Microcavity-Secondary-Flow Observation

Nika Mlinarič and Natan Osterman

***Abstract*—We propose a new type of microfluidic flow sensor, where the velocity measurements are not done on the fluid sample itself but on a second, immiscible fluid in contact with the sample. This allows us to use a low-cost, straightforward, and well-developed particle tracking velocimetry on samples otherwise unsuitable for tracer particles. Our proof-of-concept experimental setup consists of a microfluidic device with the main channel filled with the sample and rectangular side-cavities, adjacent and opened to the main channel, filled with immiscible fluid with tracer particles. The flow in the main channel induces a circular secondary flow of the cavity liquid. We observed and analyzed the side-cavity particle movement and found that its characteristic parameters show a good linear correlation with flow velocity in the main channel over the whole observed range, from approx. 600 μm/s (volumetric flow rate $\Phi_V \cong 200$ nl/min, Reynolds number $Re \cong 10^{-3}$) to approx. 3500 μm/s $\left(\Phi_V \cong 1200\ \text{nl/min}, \text{Re} \cong 10^{-2}\right)$.**

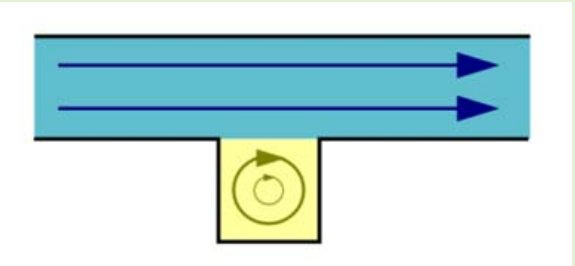

***Index Terms*—Microfluidics, flow sensor, tracer particles, droplet, secondary flow, microcavity, driven cavity, particle tracking velocimetry.**

I. Introduction

VELOCITY is one of the key parameters that characterize flow in the microfluidic circuits, and knowing it is crucial for many microfluidic applications. There is no ultimate method for measuring it in practice, but rather a wide variety of different flow sensors. To name a few, they range from sensors that utilize different variations of mechanical cantilevers [1]–[4] and Coriolis effect [5]–[8] to thermal sensors [9]–[13], electromagnetic sensors [14], sensors that utilize surface plasmon resonance [15], microwaves [16], optical tweezers [17]–[19], or track particle movement [20]–[25]. Table I shows an overview of the more common sensor types' performances, and it can be seen that cumulatively, they cover a wide range of flow rates, from about 10 nl/min up to several hundred ml/min. The proof-of-concept sensor used in our experiments is suitable for measuring low flow rates, undetectable by some of the other sensor types, and demonstrating the resolution comparable to other sensor types. Based on the principle of operation, the proposed sensor falls into the category of particle tracking velocimetry [26], [27], where one traces the movement of particles present in a liquid and calculates the flow parameters from the observed trajectories. It is one of the oldest velocimetry techniques in fluid mechanics, widely present in microfluidics, with regularly proposed adaptations and improvements. However, it has a significant downside. Tracer particles, a key aspect of the method, are not suitable for many liquid samples used in practice.

We propose a way to overcome this downside and, at the same time, demonstrate a sensor that is extremely easy to manufacture (as opposed to most of the sensor types mentioned above) and requires no special lab equipment, as detection is done with an optical microscope. It is suitable for a wide range of samples, including ones where particle presence is not acceptable and does not require the sample to heat (as with thermal sensors) or have any other unique characteristics (such as charged particles, etc.). It has a very short response time, and it provides an intuitive visual insight into the flow conditions inside the microfluidic device.

Manuscript received September 21, 2020; revised November 17, 2020; accepted November 17, 2020. Date of publication December 1, 2020; date of current version February 5, 2021. This work was supported in part by the Slovenian Research Agency, under Grant J7-8267, Grant J7-9399, and Grant P1-0192. The associate editor coordinating the review of this article and approving it for publication was Dr. Shyqyri Haxha. *(Corresponding author: Natan Osterman.)*

Nika Mlinarič was with the Faculty of Mathematics and Physics, University of Ljubljana, 1000 Ljubljana, Slovenia. She is now with AFormX Inc., 1420 Trbovlje, Slovenia.

Natan Osterman is with the Faculty of Mathematics and Physics, University of Ljubljana, 1000 Ljubljana, Slovenia, and also with the J. Stefan Institute, 1000 Ljubljana, Slovenia (e-mail: natan.osterman@ijs.si).

Digital Object Identifier 10.1109/JSEN.2020.3041792

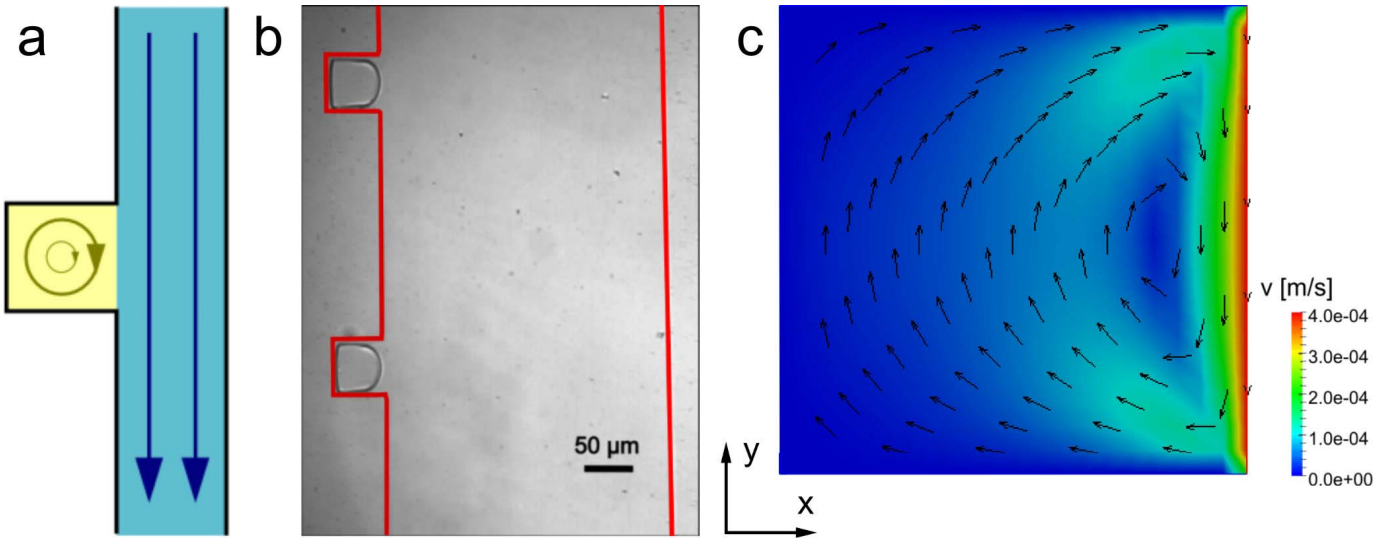

Fig. 1. (a) Schematic of the sensor. A quasi-rotational secondary flow is induced in the side microcavity. (b) Micrograph of a PDMS-filled channel with two water-filled microcavities along one of its side walls. The contrast between the channel liquid and channel walls is low, so the walls are marked with red line. (c) Numerical simulation of a 2D driven cavity flow for a cavity of 50 μm $\times$ 50 μm dimensions.

TABLE I
OVERVIEW OF MICROFLUIDIC FLOW SENSOR TYPE PERFORMANCES

Sensor type	Range	Best reported resolution/sensitivity
Mechanical cantilever	~1 µl/min – 5 ml/min	3nl/min-7µl/min,
Coriolis effect	~1 µl/min – 8 ml/min*	0.5-1%
Thermal sensors	10 nl/min – 200 ml/min	40 nl/min – 10 ml/min
Particle tracking	~1µm/s – ~1 cm/s	
Proposed concept	200 – 1200 nl/min	80 nl/min

Overview of the performances of some of the more common microfluidic flow sensor types.

* For a liquid with a density of 1000 kg/m^3.

In our experimental setup, the microfluidic device consisted of the main channel and several rectangular microcavities, adjacent and opened to the channel. The particle-free sample flows through the main channel, and the microcavities are filled with a second fluid containing dispersed particles, which is immiscible and in contact with the sample. The sample flow induces a secondary flow of the second fluid, which we measure via particle tracking velocimetry. The concept is schematically presented in Fig. 1a, and Fig. 1b shows the actual microfluidic device.

Cavities are a common element in microfluidic devices, and cavity flow in the case of one fluid flowing through both the main channel and the cavities is well-studied. On the contrary, the case with two immiscible fluids, one in each segment relevant for this experiment, has received very little attention [28].

In the single fluid case, there are essentially two cavity flow regimes, attached flow, where the streamlines "bend" into the cavity, and separated flow, which features a cavity vortex with the flow direction near the channel being the same as in the channel, and the flow direction near the cavity end being the opposite. The two regimes and the transition between them depend on the Reynolds number and cavity geometry [29]–[31]. Based on the parameters in our experiment, we expect the attached flow inside each fluid.

Furthermore, having a look at the geometry, our experiment resembles the flow in the so-called driven cavity, a well-known computational fluid dynamics test case that consists of a liquid-filled rectangular chamber with three stationary side walls and one moving sidewall. In the experiment, the moving wall is replaced by the channel flow, which exerts shear forces along the open cavity wall on the fluid-fluid interface, and gives rise to a quasi-circular secondary flow of the cavity liquid.

To illustrate the expected cavity flow, we used OpenFOAM CFD software to perform a 2D simulation of driven cavity flow, which is the simplified geometry of our experimental cavity, for a cavity of 50 μm $\times$ 50 μm cross-section. The velocity of the driven wall was representative of the velocities observed in the experiments. As in the simulation results, shown in Fig. 1c, experimentally one expects the center of the rotational flow to be shifted from the center of the cavity towards the moving wall, where the maximum flow velocity is observed. In experiments, the maximum velocities in the cavity may be lower than the flow velocities on the channel side of the interface due to slip [28]. The cavity aspect ratio 0.4 is lower than the threshold value of 0.51, so no counter-flow vortices are expected in the cavity [32], which is in good agreement with the simulation.

II. EXPERIMENT

The microfluidic channel used in the experiments was approximately 7 mm long, with a rectangular cross-section of 300 μm $\times$ 20 μm and many side cavities alongside one of its sidewalls. The height of 20 μm is a typical value for microfluidic channels, and we wanted the cavities to be the same height to simplify the manufacturing process. For the side cavity layout, we tested several rectangular designs.

We wanted a cavity where the secondary flow would be prominent, and that would produce stable droplets that would not be flushed away by the main channel flow. We have decided on a cavity of 50 μm x 50 μm. This way, the distance from the channel to the inner cavity wall (depth) was a few times larger than the height of the cavity, and the aspect ratio (depth/width) of the cavity was 1, so we did not have to study the effect of the aspect ratio. This also proved to be a right choice experimentally, as for the considerably shallower cavities with lower aspect ratios, droplets were more often flushed away by the channel flow. For considerably deeper cavities with larger aspect ratios, there would be a large portion of the droplet with low flow velocities, where the particle movement is dominated by Brownian motion, which is of no use to the sensor observations. If the cavities were placed close ($\sim$ 1 width of the cavity) apart, there were cases where the droplets in consecutive cavities stayed connected through the main channel. The cavities in the experiments were placed 250 μm apart to make sure that they did not interfere with each other.

The master mold was fabricated from SU-8 2050 negative photoresist (MicroChem, USA), using the ProtoLaser LDI (LPKF, Slovenia), a direct laser writing device. The microfluidic device was fabricated with soft lithography, using QSil 216 (ACC silicones, USA), a two-part, clear, liquid silicone. The cured polymer was bonded onto a glass base using air-plasma.

A. Liquids and Particles

The proof-of-principle demonstration required the use of two immiscible liquids, one in the channel and one in the cavity, and the presence of tracer particles in both. The particles in the cavity are part of the sensor, whereas the particles in the channel served for independent velocity measurement of the flow in the channel. For the cavity liquid, we used ultraclean water with 1 μm polystyrene spheres (FS04F, Dragon Green, Bangs Laboratories, USA). For the channel liquid, we encountered some initial problems. We tested several combinations of non-polar solvents and colloidal particles and found that in most of them, particles showed a tendency to stick to the channel walls, possibly due to electrostatic interactions, as they are less screened in non-polar liquids than in polar ones [33], [34]. We solved the problem by first mixing 1 % water dispersion of 1 μm polystyrene spheres (FS04F) with butanol (ratio 1:75) and then dispersing this into the non-polar solvent. We chose the poly(dimethylsiloxane) (PDMS), vinyldimethylsiloxy terminated (AB 109355, Abcr GmbH, Germany) as the non-polar channel liquid, and used the water – PDMS combination throughout the experiments.

B. Experimental Setup

Before the experiment, the microfluidic device was first treated with a vacuum and then soaked in ultraclean water for a few hours. This allowed the pores in QSil to fill with water (rather than air) and reduced water seeping into the surrounding QSil during the experiments. The microfluidic channel was then connected to the pressure controller (OB1 Mk3, Elveflow, France), and water with tracer particles was pumped into the channel. Next, the PDMS-particle dispersion was pumped into the channel from the same side. We adjusted the pressure and waited for the PDMS to replace the water in the channel and reach stationary conditions. We set the pressure in the channel, waited for stationary conditions, and captured a video using and an optical microscope (Axiovert 200M, Carl Zeiss, Germany) and a CMOS camera (PL-A4741, PixeLINK, USA; resolution 1280 $\times$ 1024 pixels, typical framerate 29 fps). We repeated the process for several different pressure settings.

We observed the movement of the tracer particles using 60$\times$ objective. As the field of view was not large enough to image both the channel and the cavity simultaneously, we performed a separate set of calibration measurements, where we observed only the flow in the channel to obtain a correlation between flow velocities and the pressure setting on the controller. We then moved on to the cavities, again measuring the cavity flow parameters as a function of controller pressure setting. In the last step, we combined the results obtained from the two measurement sets to analyze the properties of the flow sensor.

To measure flow velocity in the cavity at a given point, we needed to wait for one of the tracer particles to be at that point, so the measurements at each pressure setting took a few minutes and varied in length as we waited long enough to get several periods of the quasi-circular secondary flow for each setting.

C. Data Analysis

The particle trajectories were extracted from the videos with in-house developed software, optimized for this experiment. The positional accuracy for 1 μm tracer particles is better than $\pm$0.7 μm for the 20$\times$ objective and $\pm$0.4 μm for the 60$\times$ objective. With the framerate of 29 fps, this gives the conservative estimate for the absolute tracer particle velocity error of $\pm$40 μm/s (20$\times$ objective) and $\pm$23 μm/s (60$\times$ objective).

For the determination, if two sets of data were linearly correlated, we used least-squares linear fit of the form $y = kx + n$ and the correlation coefficient

$$R^2 = \frac{\left(\sum_{i=1}^{N} (x_i - \bar{x})\,(y_i - \bar{y})\right)^2}{\left(\sum_{i=1}^{N} (x_i - \bar{x})^2\right)\left(\sum_{i=1}^{N} (y_i - \bar{y})^2\right)}$$

where $\bar{x}$ and $\bar{y}$ are the mean values of x and y.

III. Results and Discussion

A. Calibration of Flow Velocity in the Channel

As discussed in the Experimental setup section, the two units, channel, and cavities were analyzed individually. First, we focused on the flow in the channel. Particle tracking velocimetry allowed us to obtain a velocity profile across the channel, and we decided to use the maximum velocity obtained at the center of the channel as a characteristic velocity for describing the flow. As expected, the velocities v_{max} are proportional to the pressure p (data is not shown).

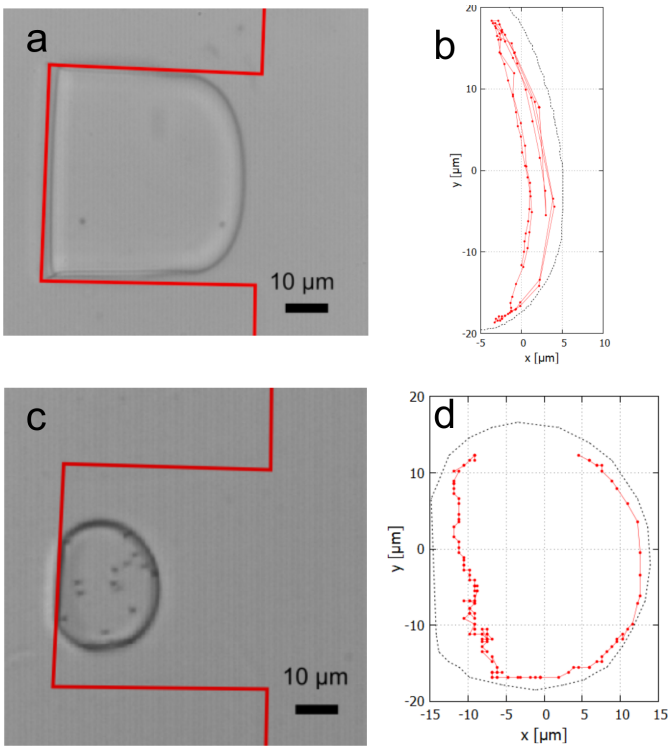

Fig. 2. Micrographs of the rectangular droplet (a) and the round droplet (c). Channel walls are marked with a red line. (b) and (d) show representative particle trajectories in droplets (a) and (c) consecutively.

Using least-square linear fit, we obtained the following relation v_{max} = (4.24±0.16) μm/(mbar s) p+ (136±23) μm/s with R^2 =0.98 for one experiment and similar values in other experiments. The offset of finite velocity at zero pressure is caused by less-than-optimal conditions at the outlet port where we had capillary attraction caused by the system that was in place to prevent the outlet port reservoir from spilling.

The channel flow velocities in the experiments were in the 600 μm/s – 3500 μm/s range with the appropriate Reynolds number for the flow in the channel from approx. $Re \cong 10^{-3}$ to approx. $Re \cong 10^{-2}$.

B. Secondary Flow in Cavities and Flow Sensor

We observed two different configurations of water droplets in cavities. First and more common (more than 90 % of cases when filling the cavities with water) was a droplet touching all three cavity walls, shown in Fig. 2a. We call this configuration a *rectangular* droplet. In less than 10 % of cases, we got so-called *round* droplets, shown in Fig. 2c, where the droplet is touching a smaller section of a sidewall.

We experimentally confirmed the occurrence of the secondary cavity flow in all of the observed droplets. While the prominence and the specifics of the flow depend significantly on the droplet geometry and its placement inside the cavity, all of the observed secondary flows exhibit a strong dependence on the controller pressure setting.

We present results for both representative cases, the rectangular droplet, and the round droplet, which were best-suited for further analysis (stable droplets, an appropriate number of particles). The first is a rectangular droplet with two tracer particles (Fig. 2a). The measurements were performed for pressure settings between 100 mbar and 500 mbar, an interval in which the quasi-circular secondary flow was prominent. Fig. 2b shows a typical particle trajectory obtained at p = 500 mbar. Similar trajectories were obtained for all pressure settings.

It can be seen that the particle travels along a section of the droplet wall touching the channel and then back in the opposite direction, this time closer to the droplet center. The movement is quasi-circular and periodical. It resembles the movement one would get in the driven cavity flow, with the center of the movement positioned close to the interface between the droplet and the channel. The dots representing the particle location are equally spaced in time (29 dots per second), and from the distances between two consecutive dots, it is clear that the tracer attains the maximum velocity alongside the interface.

The second case is a round droplet with 15 tracer particles shown in Fig. 2c. In contrast to rectangular droplets, the particle movement in round droplets is not confined to a narrow strip alongside the interface. It takes up most of the droplet area, as can be seen from the trajectory in Fig. 2d. This is due to different geometry with the section where the droplet is touching the channel wall (and where the flow velocity is equal to 0) being smaller than in the rectangular droplets.

We analyzed droplet flow characteristics and focused on two parameters that showed the most substantial dependence on the channel flow velocity – the maximum tracer velocity when tracers are traveling alongside the interface between the droplet and the channel and the frequency of the periodic loop-like tracer movement. Fig. 3 shows the dependence of the selected parameters on the channel pressure setting.

Multiple points for each pressure setting correspond to different periods of the observed movement. One can see that although the secondary flow was stationary for the whole set of measurements, the values measured vary substantially. This is because the method we use for the measurement – particle tracking – has a random element. The tracers can move perpendicular to the flow streamlines due to Brownian motion and possibly due to inertial effects [35], [36], meaning that the particle position in the flow changes between periods. This also shows one of the method's most significant drawbacks – one can only measure velocity at the tracer's position. To measure the maximum flow velocity, one would have to wait for the tracer to move to the precisely correct spot, so in theory, the measurement would need to be infinitely long. In practice, the measurements lasted for a few minutes, and we took the highest measured value as an approximation of the real value and used it in further analysis. On the graph, these maximum values of the parameters for each pressure setting are marked with red color, and only they are used in the linear fit.

Note that Fig. 3a and 3b show tracer particle velocity, which may differ from the actual flow velocity on the imaginary streamline through the particle center, due to velocity field gradient and the finite tracer size (for example, at p = 500 mbar, velocity gradient for the droplet in Fig. 2a is 170 (μm/s)/μm and the maximum velocity measured 400 μm/s).

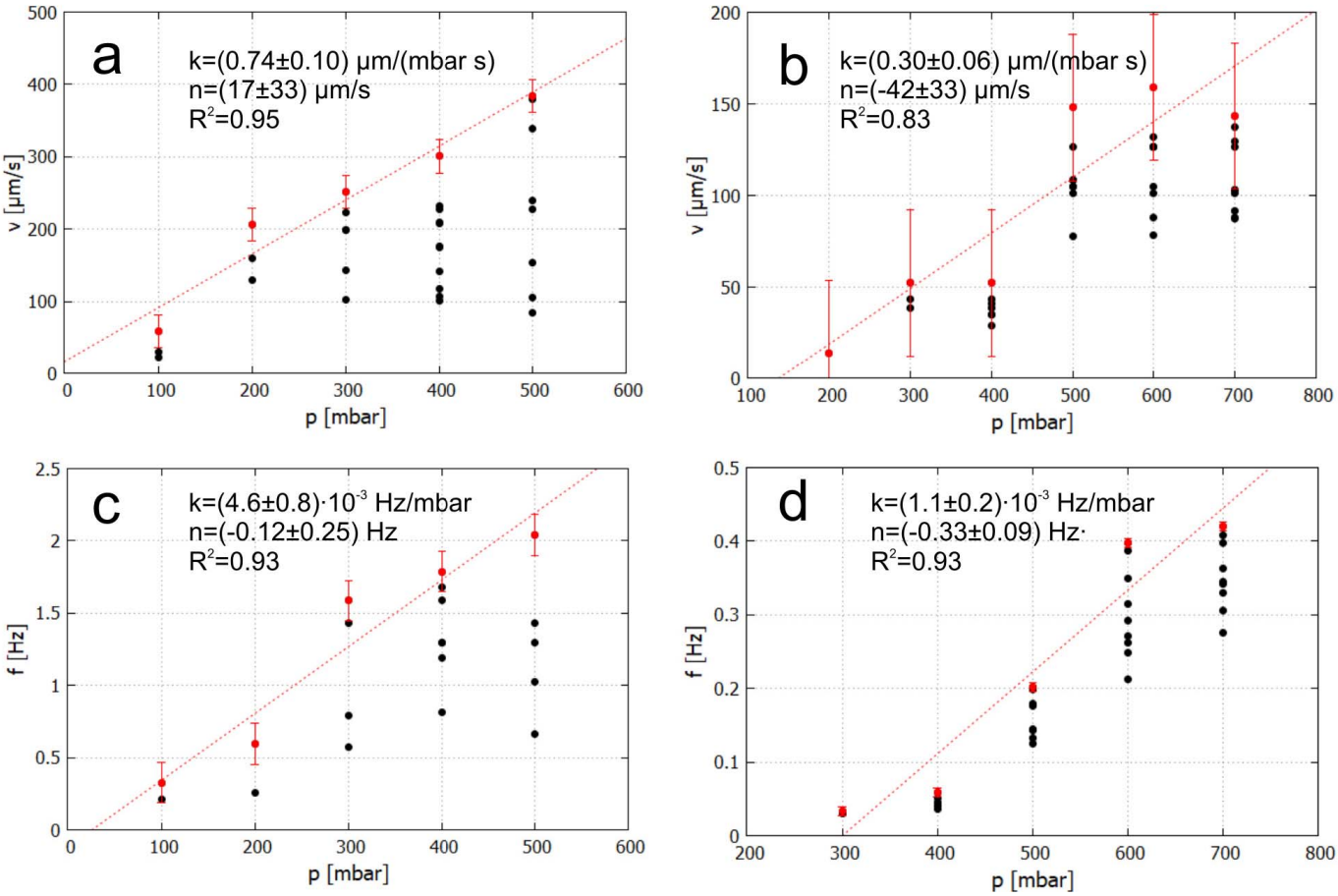

Fig. 3. Dependence of the analyzed parameters on the channel pressure for the droplets. The extreme values measured are marked in red and fitted using least square linear fit $y = kx + n$. (a) Tracer velocity along the interface for the rectangular droplet. (b) Tracer velocity along the interface for the round droplet. (c, d) Frequency of the loop-like movement of tracer particles for the rectangular and the round droplet, respectively.

The error bars for the extreme velocities account only for the error acquired during the image analysis, which originates in the error in determining the exact particle location and depends on the objective used, as explained in the previous section. Similarly, the frequency error bars account for the fact that the particle needs to be detected at the same place in two consecutive periods of movement with the software, which has finite positional accuracy, and from the frames that represent discrete points in time. The error is dependent on the time interval between two consecutive frames Δt in this manner: $\Delta f = f^2 \Delta t$.

However, we have decided to attribute the same (the maximum obtained) error to all experimental points. This is because the error from the image analysis is only one of the factors contributing to the variance of the data points. At a glance, the error bars shown in Fig. 3 are indeed small compared to the scatter of red points around the fitted line. Nevertheless, as mentioned before, the error bars only illustrate our software's accuracy for particle tracking. These errors are well defined. The spread between the fitted line and the red points not covered by the error bars can be attributed to the finite time of each measurement and the fact that the particle was not at precisely the same place in the flow for each pressure setting, so the red values are only the approximation of the real value, which we described before.

It can be seen that both analyzed parameters show a good linear correlation with the pressure setting and, therefore, the main flow velocity. The maximum particle velocities in the cavities are 5-10 times lower than the corresponding maximum velocities in the channel. When the pressure setting is changed, the new stationary flow is established in a matter of seconds.

The comparison between the square and round droplet shows different velocities and frequencies at the same pressure. This is caused by two factors. First are the conditions at the outlet port, which varied between the experiments and offset the channel velocity. And second, the location of the interface of the round droplet is moved away from the channel deeper into the cavity, which results in a decreased velocity of the channel flow at the interface.

To assess this velocity decrease, we have looked at past studies of the attached flow of fluid flowing through the main channel with side cavities [31], [32]. The geometry and Reynolds number are different from our experiments, but both studies find an exponential decay of the velocity magnitude with distance from the channel-cavity interface. The characteristic length of the decay is proportional to the

TABLE II
ASSESSMENT OF THE SENSOR ACCURACY

Droplet	Measured parameter	Absolute parameter error	Variance due to finite measurement time	Line coefficient for parameter measurement	Pressure uncertainty	Line coefficient of calibration measurement	Main channel velocity uncertainty	Main channel velocity uncertainty for infinite measurement time
Square	v	23 µm/s	18 µm/s	0.74 µm/(mbar s)	55 mbar		233 µm/s	132 µm/s
Round	v	40 µm/s	0	0.30 µm/(mbar s)	133 mbar	4.24 µm/(mbar s)	564 µm/s	564 µm/s
Square	f	0.14 Hz	0.16 Hz	$4.6 \cdot 10^{-3}$ Hz/mbar	65 mbar		277 µm/s	129 µm/s
Round	f	0.006 Hz	0.06 Hz	$1.1 \cdot 10^{-3}$ Hz/mbar	60 mbar		254 µm/s	23 µm/s

Assessment of the accuracy of the proof of concept sensor in our experiments

cavity's width and also depends on other parameters. In the study [31], which was conducted for $Re = 3$, and a similar aspect ratio than in our experiments, the velocity magnitude of the flow half-way deep into the cavity is approximately *1/5* of the velocity magnitude at the channel – cavity interface. While the conditions in our experiment are not precisely the same, because our cavity is not filled only with the fluid from the main channel, but also contains a droplet of an immiscible fluid, the above can still provide an insight into the flow characteristics and shows that the decrease of the velocity is significant, if the droplet surface is moved deeper into the cavity. This consequently decreases the sensitivity of the sensor.

We find that the biggest shortcoming of the proposed concept is that every moment, velocity can only be measured at the tracer particles' positions. With low particle concentrations, there are periods of time, especially in the rectangular droplets, where all of the particles are in the proximity of the cavity wall opposite from the channel. The low velocity there is too low, and the Brownian motion is dominant. To measure the absolute maximum velocity in the cavity, the measurement would have to last infinitely long. To shorten the necessary time, one could increase particle concentration, but this adds to the complexity of extracting particle trajectories or flow parameters in the post-processing. Possible intra-particle interactions should also be considered.

We assessed our experimental sensor concept's accuracy in the following way (Table II): first, we need a metric that describes the uncertainty of parameter measurement. We divide it into two contributions – the absolute parameter error, represented with error bars in Fig. 3, which is characteristic of the particle tracking software and is the minimum uncertainty possible in the experiments, and the uncertainty one would get with infinitely long measurement time. It is shown in column 3. Moreover, the second contribution is the consequence of the finite time of the measurements and the observed particle's changing position in the secondary flow, which contributes to the additional variance of the red dots around the fitted line, shown in column 4. We have estimated this contribution from the furthest outlier position for each parameter measurement in Fig. 3.

We then divide the uncertainty (sum of both contributions) with the coefficient of the fitted line for each measurement in Fig. 3 (column 5), so we get the estimate of the pressure uncertainty (column 6). We multiplied it by the average line coefficient from the calibration measurements (column 7) and get the estimated uncertainty for flow velocity in the main channel, shown in column 8. Additionally, column 9 shows the theoretical flow velocity uncertainty if there would be no variance contribution.

We see that the finite time of the measurements played a much larger role in frequency measurements than in velocity measurements, where the minutes-long intervals gave us representative values of parameters.

IV. CONCLUSION

We presented the results of the proof-of-concept experiment of a new flow rate sensor. We demonstrated that the secondary flow in the side cavity is indeed induced and that it can be observed using particle tracking velocimetry. The analyzed parameters show a good linear correlation with the channel flow velocity over the whole measured velocity range from approx. 600 μm/s to approx. 3500 μm/s, with the corresponding volumetric flow rates from approx. 200 nl/min to approx. 1200 nl/min.

The shape of the droplets (rectangular or round) affect the shape of the induced secondary flow, and the position of the droplet surface inside the cavity affects the maximum velocity of the induced flow.

One of the observed parameters is the frequency of the periodic movement of tracer particles, which opens up a possibility to omit the optical microscope and camera and implement an optical sensor that would sense when the particle crosses a certain point directly on a chip, making the sensor more compact and portable. The sensor sensitivity may be improved with different geometric designs – we have observed secondary flow in droplets trapped inside the main channel for the pressure settings as low as 16 mbar, but said droplets were too unstable for further analysis. We have obtained a set of velocity measurements in a square droplet in the range of 40 – 100 mbar, with a strong linear correlation between particle velocity and pressure similar to Fig. 3a, but there was no periodic movement because the flow velocities away from the fluid interface were too low. The main channel velocity (column 8 of Table II) for that experiment was 56 μm/s.

Different liquids could be used with almost no modification – the main requirement is that they are immiscible, while the slip condition at the fluid interface should be further studied for different liquid combinations. Viscosity should also be considered, as increased viscosity of the channel liquid would decrease the velocity at the same pressure setting and sensor geometry, and the viscosity of the

cavity liquid would affect the prominence of the secondary flow.

The design with side cavities can be applied to different geometries of the main channel. The secondary flow parameters depend directly on velocity (as opposed to the flow rate), so it is relatively insensitive to the channel geometry. The height of the channel (and subsequently the cavity) needs to be considerably larger than the size of the tracer particles so that they can move unobstructed. The velocity of the flow in the main channel is an important parameter, as it needs to be large enough that the movement of the particles in the cavity is dominated by the flow, not by the Brownian motion. For applications with channel flow velocities too high or too low, the main channel could be widened or made narrower at the section where the cavity is so that the flow velocity decreases or increases to the desired range. The sensor response was linear throughout the observed range for the range tested in the proof of concept experiment.

The presented sensor concept is non-invasive as it is physically separated from the sample liquid; it is inexpensive, easy to manufacture, works in a broad temperature range, and does not require heating of the sample; it is sample-insensitive as the only constraint is that the liquid utilized in the sensor must not mix with the sample. Given the flexibility and ease of implementation, we anticipate that the sensor could be widely used as a functional block in microfluidic circuits.

References

[1] V. Lien and F. Vollmer, "Microfluidic flow rate detection based on integrated optical fiber cantilever," *Lab Chip*, vol. 7, no. 10, p. 1352, 2007, doi: 10.1039/b706944h.

[2] N. Noeth, S. S. Keller, and A. Boisen, "Fabrication of a cantilever-based microfluidic flow meter with nL min^{-1} resolution," *J. Micromech. Microeng.*, vol. 21, no. 1, Jan. 2011, Art. no. 015007, doi: 10.1088/0960-1317/21/1/015007.

[3] A. S. Nezhad, M. Ghanbari, C. G. Agudelo, M. Packirisamy, R. B. Bhat, and A. Geitmann, "PDMS microcantilever-based flow sensor integration for lab-on-a-chip," *IEEE Sensors J.*, vol. 13, no. 2, pp. 601–609, Feb. 2013, doi: 10.1109/JSEN.2012.2223667.

[4] M. S. Cheri, H. Latifi, J. Sadeghi, M. S. Moghaddam, H. Shahraki, and H. Hajghassem, "Real-time measurement of flow rate in microfluidic devices using a cantilever-based optofluidic sensor," *Analyst*, vol. 139, no. 2, pp. 431–438, 2014, doi: 10.1039/C3AN01588B.

[5] R. Smith, D. R. Sparks, D. Riley, and N. Najafi, "A MEMS-based coriolis mass flow sensor for industrial applications," *IEEE Trans. Ind. Electron.*, vol. 56, no. 4, pp. 1066–1071, Apr. 2009, doi: 10.1109/TIE.2008.926703.

[6] J. Haneveld *et al.*, "Modeling, design, fabrication and characterization of a micro coriolis mass flow sensor," *J. Micromech. Microeng.*, vol. 20, no. 12, Dec. 2010, Art. no. 125001, doi: 10.1088/0960-1317/20/12/125001.

[7] W. Sparreboom *et al.*, "Compact mass flow meter based on a micro coriolis flow sensor," *Micromachines*, vol. 4, no. 1, pp. 22–33, Mar. 2013, doi: 10.3390/mi4010022.

[8] R. Monge, J. Groenesteijn, D. Alveringh, R. J. Wiegerink, J. Lötters, and L. J. Fernandez, "SU–8 micro coriolis mass flow sensor," *Sens. Actuators B, Chem.*, vol. 241, pp. 744–749, Mar. 2017, doi: 10.1016/j.snb.2016.10.133.

[9] R. Vilares *et al.*, "Fabrication and testing of a SU-8 thermal flow sensor," *Sens. Actuators B, Chem.*, vol. 147, no. 2, pp. 411–417, Jun. 2010, doi: 10.1016/j.snb.2010.03.054.

[10] H. Berthet, J. Jundt, J. Durivault, B. Mercier, and D. Angelescu, "Time-of-flight thermal flowrate sensor for lab-on-chip applications," *Lab Chip*, vol. 11, no. 2, pp. 215–223, 2011, doi: 10.1039/C0LC00229A.

[11] J. T. W. Kuo, L. Yu, and E. Meng, "Micromachined thermal flow sensors—A review," *Micromachines*, vol. 3, no. 3, pp. 550–573, Jul. 2012, doi: 10.3390/mi3030550.

[12] Y. Li, G. Yan, L. Zhang, and S. He, "Microfluidic flowmeter based on micro 'hot-wire' sandwiched Fabry-Perot interferometer," *Opt. Exp.*, vol. 23, no. 7, p. 9483, Apr. 2015, doi: 10.1364/OE.23.009483.

[13] C.-H. Wu, D. Kang, P.-H. Chen, and Y.-C. Tai, "MEMS thermal flow sensors," *Sens. Actuators A, Phys.*, vol. 241, pp. 135–144, Apr. 2016, doi: 10.1016/j.sna.2016.02.018.

[14] S. Sengupta, B. Ziaie, and V. H. Barocas, "Lag-after-pulsed-separation microfluidic flowmeter for biomacromolecular solutions," *Sens. Actuators B, Chem.*, vol. 99, no. 1, pp. 25–29, Apr. 2004, doi: 10.1016/j.snb.2003.08.017.

[15] S. Deng *et al.*, "A novel microfluidic flow rate detection method based on surface plasmon resonance temperature imaging," *Sensors*, vol. 16, no. 7, p. 964, Jun. 2016, doi: 10.3390/s16070964.

[16] M. H. Zarifi, H. Sadabadi, S. H. Hejazi, M. Daneshmand, and A. Sanati-Nezhad, "Noncontact and nonintrusive microwave-microfluidic flow sensor for energy and biomedical engineering," *Sci. Rep.*, vol. 8, no. 1, p. 139, Dec. 2018, doi: 10.1038/s41598-017-18621-2.

[17] C.-L. Lin, I. Wang, B. Dollet, and P. L. Baldeck, "Velocimetry microsensors driven by linearly polarized optical tweezers," *Opt. Lett.*, vol. 31, no. 3, p. 329, 2006, doi: 10.1364/OL.31.000329.

[18] R. D. Leonardo, J. Leach, H. Mushfique, J. M. Cooper, G. Ruocco, and M. J. Padgett, "Multipoint holographic optical velocimetry in microfluidic systems," *Phys. Rev. Lett.*, vol. 96, no. 13, Apr. 2006, Art. no. 134502, doi: 10.1103/PhysRevLett.96.134502.

[19] P. Almendarez-Rangel, B. Morales-Cruzado, E. Sarmiento-Gómez, R. Romero-Méndez, and F. G. Pérez-Gutiérrez, "A microflow velocity measurement system based on optical tweezers: A comparison using particle tracking velocimetry," *Eur. J. Mech. B/Fluids*, vol. 72, pp. 561–566, Nov. 2018, doi: 10.1016/j.euromechflu.2018.08.004.

[20] R. J. Adrian, "Twenty years of particle image velocimetry," *Experim. Fluids*, vol. 39, no. 2, pp. 159–169, Aug. 2005, doi: 10.1007/s00348-005-0991-7.

[21] S. Kim and S. J. Lee, "Measurement of 3D laminar flow inside a micro tube using micro digital holographic particle tracking velocimetry," *J. Micromech. Microeng.*, vol. 17, no. 10, pp. 2157–2162, Oct. 2007, doi: 10.1088/0960-1317/17/10/030.

[22] K.-S. Im, K. Fezzaa, Y. J. Wang, X. Liu, J. Wang, and M.-C. Lai, "Particle tracking velocimetry using fast X-ray phase-contrast imaging," *Appl. Phys. Lett.*, vol. 90, no. 9, Feb. 2007, Art. no. 091919, doi: 10.1063/1.2711372.

[23] R. Lindken, M. Rossi, S. Große, and J. Westerweel, "Micro-particle image velocimetry (μPIV): Recent developments, applications, and guidelines," *Lab Chip*, vol. 9, no. 17, p. 2551, 2009, doi: 10.1039/b906558j.

[24] C. Cierpka, B. Lütke, and C. J. Kähler, "Higher order multi-frame particle tracking velocimetry," *Exp. Fluids*, vol. 54, no. 5, p. 1533, May 2013, doi: 10.1007/s00348-013-1533-3.

[25] P. Memmolo *et al.*, "Recent advances in holographic 3D particle tracking," *Adv. Opt. Photon.*, vol. 7, no. 4, p. 713, Dec. 2015, doi: 10.1364/AOP.7.000713.

[26] T. Dracos, "Particle tracking velocimetry (PTV)," in *Three-Dimensional Velocity and Vorticity Measuring and Image Analysis Techniques* (Lecture Notes from the Short Course Held), T. Dracos, Ed. Dordrecht, The Netherlands: Springer, Sep. 1996, pp. 155–160.

[27] S. J. Williams, C. Park, and S. T. Wereley, "Advances and applications on microfluidic velocimetry techniques," *Microfluidics Nanofluidics*, vol. 8, no. 6, pp. 709–726, Jun. 2010, doi: 10.1007/s10404-010-0588-1.

[28] C. Schönecker and S. Hardt, "Longitudinal and transverse flow over a cavity containing a second immiscible fluid," *J. Fluid Mech.*, vol. 717, pp. 376–394, Feb. 2013, doi: 10.1017/jfm.2012.577.

[29] Z. T. F. Yu, Y.-K. Lee, M. Wong, and Y. Zohar, "Fluid flows in microchannels with cavities," *J. Microelectromech. Syst.*, vol. 14, no. 6, pp. 1386–1398, Dec. 2005, doi: 10.1109/JMEMS.2005.859086.

[30] R. Fishler, M. K. Mulligan, and J. Sznitman, "Mapping low-Reynolds-number microcavity flows using microfluidic screening devices," *Microfluidics Nanofluidics*, vol. 15, no. 4, pp. 491–500, Oct. 2013, doi: 10.1007/s10404-013-1166-0.

[31] F. Shen, P. Xiao, and Z. Liu, "Microparticle image velocimetry (μPIV) study of microcavity flow at low Reynolds number," *Microfluidics Nanofluidics*, vol. 19, no. 2, pp. 403–417, Aug. 2015, doi: 10.1007/s10404-015-1575-3.

[32] N. Osterman, J. Derganc, and D. Svenšek, "Formation of vortices in long microcavities at low Reynolds number," *Microfluidics Nanofluidics*, vol. 20, no. 2, pp. 1–10, Feb. 2016, doi: 10.1007/s10404-015-1689-7.

[33] M. F. Hsu, E. R. Dufresne, and D. A. Weitz, "Charge stabilization in nonpolar solvents," *Langmuir*, vol. 21, no. 11, pp. 4881–4887, May 2005, doi: 10.1021/la046751m.

[34] S. K. Sainis, V. Germain, C. O. Mejean, and E. R. Dufresne, "Electrostatic interactions of colloidal particles in nonpolar solvents: Role of surface chemistry and charge control Agents," *Langmuir*, vol. 24, no. 4, pp. 1160–1164, Feb. 2008, doi: 10.1021/la702432u.

[35] P. G. Saffman, "The lift on a small sphere in a slow shear flow," *J. Fluid Mech.*, vol. 22, no. 2, pp. 385–400, Jun. 1965, doi: 10.1017/S0022112065000824.

[36] T. M. Geislinger and T. Franke, "Hydrodynamic lift of vesicles and red blood cells in flow—From Fåhræus & Lindqvist to microfluidic cell sorting," *Adv. Colloid Interface Sci.*, vol. 208, pp. 161–176, Jun. 2014, doi: 10.1016/j.cis.2014.03.002.

Nika Mlinarič received the B.S. and M.S. degrees in physics from the Faculty of Mathematics and Physics, University of Ljubljana, Slovenia, in 2015 and 2018, respectively. Her master's thesis was in the field of microfluidics. Since 2017, she has been working full-time as an Aerospace Engineer at AFormX Aviation Technology and Precision Mechanics, Trbovlje, Slovenia. Her primary focus is the development of virtual reality flight simulators. She is also involved in projects in the field of computational analysis and brain–computer-interface. She was part of the AFormX team that received Golden Innovation Award for VR flight simulators for basic pilot training from the Chamber of Commerce and Industry of Slovenia in 2017, and won Light Aircraft Design Competition held by the Royal Aeronautical Society in 2019. In 2019, she was one of the ten nominees of the Woman Engineer of the Year, a national selection aiming to promote women in STEM.

Natan Osterman graduated in 2004. He received the Ph.D. degree in physics from the University of Ljubljana, Slovenia, in 2009. As a Postdoctoral Researcher, he worked at the J. Stefan Institute (Ljubljana, Slovenia) and the Ludwig Maximilian University of Munich (Germany). Since 2015, he has been an Assistant Professor with the Faculty of Mathematics and Physics, University of Ljubljana, where he has been giving lectures in classical physics and experimental methods in biophysics. His research is in the fields of experimental soft matter physics.